JOURNAL OF GEOPHYSICAL RESEARCH, VOL. ???, XXXX, DOI:10.1029/,

Magnetohydrodynamic Simulation of the Interaction between Interplanetary Strong Shock and Magnetic Cloud and its Consequent Geoeffectiveness

Ming Xiong, Huinan Zheng, Yuming Wang, and Shui Wang

CAS Key Laboratory for Basic Plasma Physics, School of Earth and Space

Sciences, University of Science and Technology of China, Hefei, Anhui

230026, China

Ming Xiong, Huinan Zheng, Yuming Wang, and Shui Wang, CAS Key Laboratory for Basic Plasma Physics, School of Earth and Space Sciences, University of Science and Technology of China, Hefei, Anhui 230026, China (mxiong@mail.ustc.edu.cn; hue@ustc.edu.cn; ymwang@ustc.edu.cn; and swan@ustc.edu.cn)

Abstract. Numerical studies have been performed to interpret the observed "shock overtaking magnetic cloud (MC)" event by a 2.5 dimensional magnetohydrodynamic (MHD) model in heliospheric meridional plane. Results of an individual MC simulation show that the MC travels with a constant bulk flow speed. The MC is injected with very strong inherent magnetic field over that in the ambient flow and expands rapidly in size initially. Consequently, the diameter of MC increases in an asymptotic speed while its angular width contracts gradually. Meanwhile, simulations of MC-shock interaction are also presented, in which both a typical MC and a strong fast shock emerge from the inner boundary and propagate along heliospheric equator, separated by an appropriate interval. The results show that the shock firstly catches up with the preceding MC, then penetrates through the MC, and finally merges with the MC-driven shock into a stronger compound shock. The morphologies of shock front in interplanetary space and MC body behave as a central concave and a smooth arc respectively. The compression and rotation of magnetic field serve as an efficient mechanism to cause a large geomagnetic storm. The MC is highly compressed by the the overtaking shock. Contrarily, the transport time of incidental shock influenced by the MC depends on the interval between their commencements. Maximum geoeffectiveness results from that when the shock enters the core of preceding MC, which is also substantiated to some extent by a corresponding simplified analytic model. Quantified by *Dst* index, the specific result gives that the geoeffec-

tiveness of an individual MC is largely enhanced with 80% increment in maximum by an incidental shock.

1. Introduction

Coronal mass ejection (CME) is one of the most frequently eruptive phenomena in solar atmosphere, which causes significant changes in coronal structure accompanied by observable mass outflow. A great deal of CME observation data has been accumulated by spacecraft OSO-7, Skylab, P78-1, SMM, ISEE3, Helios, Yohkoh, SOHO, Ulysses, Wind, ACE et al. over the past 30 years. A typical CME is launched into interplanetary (IP) space with magnetic flux of 10^{23}maxwell and plasma mass of 10^{16}g [Gosling, 1990; Webb et al., 1994]. The "solar flare myth" that CMEs have no fundamental association (in terms of cause and effect) with flares [Gosling, 1993; Gosling and Hundhausen, 1995] is quite controversial [e.g., Svestka, 1995; Dryer, 1996]. It is more favorable of the equal importance of CME and flare concerning the source of IP transient disturbances and non-recurrent geomagnetic storms [Dryer, 1996]. Statistical research shows that nearly half of all CMEs form magnetic clouds (MCs) in IP space [Klein and Burlaga, 1982; Cane et al., 1997]. MC is very concerned in space community, because its regular magnetic field with large southward magnetic component always leads to geomagnetic storm. The characteristics of MCs, as defined by Burlaga et al. [1981], are enhanced magnetic field, smooth rotation of the magnetic field, low proton temperature, and a low ratio of proton thermal to magnetic pressure β_p. Many studies modeled an MC by an ideal local cylinder with a force-free field [e.g., Goldstein, 1983; Burlaga, 1988; Farrugia et al., 1993; Kumar and Rust, 1996; Osherovich and Burlaga, 1997], though in real situation an MC should probably be a curved loop-like structure with its feet connecting to the solar surface [Larson et al., 1997]. Numerical simulations have been carried out to investigate the behavior of isolated loop-like MCs with various magnetic field strengths, axis orientations and speeds, based on the flux rope model [e.g., Vandas et al., 1995, 1996a, b, c, 1997a, b; Vandas and Odstrcil, 2000; Vandas et al., 2002; Groth et al., 2000; Odstrcil et al., 2002; Schmidt and Cargill, 2003; Vandas, 2003; Manchester et al., 2004a, b]. A great consistency was found between the in-situ observations, theoretical analyses and numerical simulations.

Recent studies have focused on the existence of more complex structure, with less defined characteristics and a possible association with interactions among CMEs, shocks, MCs, and corotating regions, such as complex ejecta [Burlaga et al., 2002], multiple MCs [Wang et al., 2002, 2003a], shock-penetrated MCs [Wang et al., 2003b; Berdichevsky et al., 2005], and so on. Most of the different physical phenomena, which are likely to occur during the propagation of a following faster CME overtaking a preceding slower CME, have been studied by both 2.5-dimensional (2.5D) and 3-dimensional (3D) magnetohydrodynamic (MHD) numerical simulations: the interaction of a shock wave with an MC [Vandas et al., 1997a; Odstrcil et al., 2003], the interaction of two MCs [Odstrcil et al., 2003; Gonzalez-Esparza et al., 2004; Lugaz et al., 2005; Wang et al., 2005], and the acceleration of electrons associated with the shock-cloud interaction [Vandas and Odstrcil, 2004].

The establishment of space weather forecasting system is ongoing as urgently needed by human civilization. Numerical MHD model may play a critical role in it [Dryer, 1998]. IP medium is a pivotal node in cause-effect chains of solar-terrestrial transporting events. The correlation between Dst index and various IP parameters have been comprehensively studied [e.g., Burton et al., 1975; Vassiliadis et al., 1999] and applied in related numerical simulations [e.g., Vandas, 2003]. Moreover, some observation-data-driven numerical models have already been applied in the real time “fearless forecasting”: (1) HAF

(Hakamada-Akasofu-Fry) model based on kinetics [Fry et al., 2001, 2005; Intriligator et al., 2005; McKenna-Lawlor et al., 2005]; (2) STOA (Shock Time of Arrival) based on classical self-similarity blast wave theory [Smart and Shea, 1985]; (3) ISPM (Interplanetary Shock Propagation Model) based on 2.5D MHD simulation [Smith and Dryer, 1990]; (4) an ensemble of above three models [Dryer et al., 2001, 2004; McKenna-Lawlor et al., 2002; Fry et al., 2003, 2004].

The observed "shock overtaking MC" event complicates IP dynamics. With an enough strong magnitude, a fast shock can propagate through a low β MC and survive as a discontinuity in front part of the MC. It can even penetrate the MC and merge with the original MC-driven shock into a stronger compound shock. The evolution stages of MC-shock interaction detected by Wind and ACE spacecraft at 1 AU may be reduced into two categories: (1) shock still in MC, such as October 3-6 2000 and November 5-7 2001 events [Wang et al., 2003b]; (2) shock ahead of MC after completely penetrating it, such as March 20-21 2003 event [Berdichevsky et al., 2005]. Ruling out the possibility of weak shock dissipation in low β MC plasma, the MC-shock compound at 1 AU changes from category 1 to 2, as their eruption interval decreases at solar corona. MC-shock interaction is also an IP cause of large geomagnetic storms [Wang et al., 2003b, c]. Obviously MC with a penetrating shock at various stages may result in different geoeffectiveness.

In this paper, studies are presented to understand the dynamic process of the "shock overtaking MC" event and its effect on geomagnetic storm strength by numerical simulation based on a 2.5D ideal MHD model. A brief description of the MHD equations and the numerical scheme used to solve them, as well as the steady state solar wind, the MC configuration and shock specification, is given in Section 2. Simulation results of an individual MC are described in Section 3. Results of MC-shock interaction are discussed and analyzed in Section 4. The geoeffectiveness of MC-shock interaction is discussed in Section 5. Finally, conclusions are summarized in Section 6.

2. Numerical MHD Model

2.1. Governing MHD Equations

The macro-scope behavior of magnetized plasma can be well described with MHD equations by using the conservation laws, supplemented by the equation of state of fluids and divergence-free condition of magnetic field. Since IP magnetic field (IMF) co-rotates with the Sun, it is convenient to adopt a co-rotating coordinate system, in which the fluid velocity is parallel to the magnetic field. With the assumption of an ideal gas with a polytropic index $\gamma = 5/3$ and neglecting the effects of viscosity, electrical resistivity, and thermal conduction, the ideal MHD equations are written as follows (cf. Jeffrey and Taniuti [1964]).

$$\frac{\partial \rho}{\partial t} + \nabla \cdot (\rho \mathbf{v}) = 0 \tag{1}$$

$$\frac{\partial (\rho \mathbf{v})}{\partial t} + \nabla \cdot \left[\rho \mathbf{v}\mathbf{v} + \left(p + \frac{1}{8\pi} B^2 \right) I - \frac{1}{4\pi} \mathbf{B}\mathbf{B} \right] = \mathbf{f} \tag{2}$$

$$\frac{\partial \mathbf{B}}{\partial t} - \nabla \times (\mathbf{v} \times \mathbf{B}) = 0 \tag{3}$$

$$\begin{aligned} \frac{\partial W}{\partial t} + \nabla \cdot \left[\left(\frac{\gamma}{\gamma - 1} p + \frac{1}{2} \rho v^2 \right) \mathbf{v} + \frac{1}{4\pi} \mathbf{B} \times (\mathbf{v} \times \mathbf{B}) \right] \\ = \mathbf{f} \cdot \mathbf{v} \end{aligned} \tag{4}$$

with

$$\begin{aligned} \mathbf{f} &= -\rho \left[\frac{g R_s^2}{r^2} \frac{\mathbf{r}}{r} + \mathbf{\Omega} \times (\mathbf{\Omega} \times \mathbf{r}) + 2(\mathbf{\Omega} \times \mathbf{v}) \right] \\ W &= \frac{1}{2} \rho v^2 + \frac{1}{8\pi} B^2 + \frac{p}{\gamma - 1}. \end{aligned}$$

Where ρ is the plasma mass density, $\mathbf{v}$ the plasma velocity, $\mathbf{B}$ the magnetic field, p the plasma pressure (sum of electron and proton pressures), $\mathbf{\Omega}$ the angular speed of solar rotation ($= 2.9 \times 10^{-6}$ rad/s), I the unit matrix, R_s the solar radius, g the gravitational acceleration at the solar surface. Equations (1)-(4) are expressed in spherical coordinate system (r, θ, φ), dealing with 2.5D problems in the meridional plane. Namely, the partial derivatives of all dependent variables with respect to azimuthal angle φ are zero.

2.2. Computational Techniques

The mathematical connotation of shock overtaking MC belongs to high resolution problems for the interaction between discontinuity and complex smooth structure. Total variation diminishing (TVD) scheme, a shock-capturing method, is applied to numerically solve MHD equations [Harten, 1983; Ryu and Jones, 1995], which possesses a formal accuracy of the second order in smooth flow regions except at extreme points. An 8 wave model [Powell et al., 1995] is adopted to guarantee divergence-free condition of magnetic field.

Furthermore, the magnetic flux function ψ is introduced to ensure the accuracy of magnetic field in the region near the shock front and the MC, which satisfies

$$\frac{\partial \psi}{\partial t} + v_r \frac{\partial \psi}{\partial r} + \frac{v_\theta}{r} \frac{\partial \psi}{\partial \theta} = 0 \tag{5}$$

with

$$\mathbf{B} = \left(\frac{1}{r^2 \sin\theta} \frac{\partial \psi}{\partial \theta}, -\frac{1}{r \sin\theta} \frac{\partial \psi}{\partial r}, B_\varphi \right). \tag{6}$$

Equation (5) is solved by fifth order weighted essentially non-oscillation (WENO) scheme [Shu, 1997] and the meridional components of magnetic field are updated by ψ in equation (6). In addition, special techniques in the numerical simulations of magnetic flux rope

[Hu et al., 2003; Zhang et al., 2005] are introduced here, which eliminate the numerical reconnection across the heliosphere current sheet (HCS) and guarantee the conservations of mass, axial and toroidal magnetic fluxes of magnetic rope.

For simulations in this paper, computational domain is taken to be $25R_s \leq r \leq 300R_s$, $0^\circ \leq \theta \leq 180^\circ$ and discretized in meshes evenly spaced with $\Delta r = 1.5R_s$ and $\Delta\theta = 1.5^\circ$. To avoid the complex boundary conditions associated with transonic flow, the inner boundary of computational domain is chosen so that the solar wind speed has already exceeded the fast magnetoacoustic speed. Since all waves are entering the domain at the inner boundary ($r = 25R_s$), all quantities can be specified independently. While linear extrapolations are exerted at the outer boundary ($r = 300R_s$) where all waves exit the domain. Symmetric conditions are used at latitudinal directions.

2.3. Ambient Solar Wind Equilibrium

Ambient solar wind equilibrium is obtained simply by specifying the inner boundary conditions. A unique steady state solar wind solution is obtained after ~ 120 hours by fixing a set of parameters at the inner boundary, with proton number density $N_p = 550$ cm^{-3}, radial solar wind speed $v_r = 375$ kms^{-1}, magnetic field strength $B = 400$ nT, the plasma beta (defined as the ratio of plasma thermal to magnetic pressure) $\beta = \frac{8\pi p}{B^2} = 0.23$, as well as the conditions $B_\theta = 0$ and $\mathbf{v} \parallel \mathbf{B}$. The configuration is quite similar to that by Wang et al. [2005], with its typical values at $25R_s$ (the inner boundary) and $213R_S$ (near the earth orbit) listed in Table 1. An HCS is introduced by simply reversing the magnetic field across the equator, i.e. magnetic field directs outwards (inwards) in southern (northern) semi-heliosphere. Theoretically, the HCS is an ideal tangential discontinuity in MHD macro-scale, but it is here smeared out over several grids by numerical diffusion.

However this slightly smeared structure is quite similar to the configuration that an HCS is embedded in a relatively thicker heliospheric plasma sheet (HPS), which is substantiated by space observation during solar minimum [Winterhalter et al., 1994]. In addition, the equilibrium here does not resemble the bimodal nature of the solar wind with fast flow over the poles and slow flow at low latitudes. We argue that this will not distort the fundamental physical process of the MC-shock interaction, which locates mainly at low latitudes. The ambient equilibrium is described as slow solar wind astride HCS–HPS.

2.4. Specification of MC and Shock Emergences

Specific methods for MC injection by Vandas et al. [1995] and fast shock injection by Hu [1998]; Hu and Jia [2001] are applied in our simulation through the inner boundary condition modification. Once MC or shock is completely emerged into IP medium, the original inner boundary condition as mentioned in Section 2.3 is restored.

The magnetic field configuration of an MC is described as Lundquist solution in local cylindrical coordinate (R, Φ, Z) [Lundquist, 1950].

$$\begin{cases} B_R = 0 \\ B_\Phi = B_0 H J_1(\alpha R) \\ B_Z = B_0 J_0(\alpha R) \end{cases} \tag{7}$$

where B_0 specifies the magnetic field magnitude at MC core, H is the magnetic helicity, $\alpha = 2.4/R_m$ and R_m is MC radius. With given emergence time t_m, mass M_m, speed v_m, radius R_m, plasma β, and helicity H together with above magnetic configuration, an MC is uniquely determined. It is unrealistic to approximate the 3D structure of an MC that is rooted deeply in solar surface in 2.5D coordinate system. However, regarding MC as a section of the 3D magnetic loop, its dynamic characteristics could still be reflected by a 2.5D numerical simulation.

An incidental fast shock is characterized by several parameters: its emergence time t_{s0}, the latitude of its center θ_{sc}, the latitudinal width of its flank $\Delta\theta_s$, the maximum ratio of total pressure (sum of thermal and magnetic pressures) at shock center R^*, the duration of growth, maintenance and recovery phases (t_{s1}, t_{s2}, t_{s3}). The ratio of total pressure decreases from R^* at center to 1 at both flank edges as cosine function of the angle. It varies linearly with time during the growth and recovery phases of shock disturbance. Given the upstream state at the inner boundary and R^*, downstream state is derived by Rankine–Hugoniot relationship. The introduced shocks in our simulation are strong enough to be faster than the local magnetosonic speed at all time. A shock can be formed closer to the sun, below the usually-computed steady-state critical points. Many solar observations show that shock can be formed below Alfvén critical point which is below the inner boundary of the computational domain [e.g., Cliver et al., 2004; Raouafi et al., 2004; Cho et al., 2005].

3. Propagation of an Individual MC (Case A)

We present here an individual MC simulation firstly, to manifest its characteristics, as well as for comparison with MC-shock interaction in the next section. The MC emerges along HCS from the inner boundary. It takes the following parameters referring to Equation (7),

$$R_m = 5R_s, \quad B_0 = 1700 \text{ nT}, \quad H = 1$$

and

$$v_m = 530 \text{ kms}^{-1}, \quad M_m = 4.8 \times 10^{12} \text{ kg}, \quad \beta = 0.02.$$

Magnetic flux function ψ (cf. Equation (6)) is 1.51×10^{14} Wb at the core of MC, comparing with 1.12×10^{14} and 0 Wb in HCS and heliospheric poles, respectively. The axial magnetic flux of MC is calculated to be 2.5×10^{13} Wb. This MC and its surrounding IMF have the same magnetic polarity in meridional plane.

The simulation of an MC passing nearby the Lagrangian point (L1) is shown in Figure 1. Under each image are two corresponding radial profiles by cutting right through 0° (noted by Lat. = 0°) and 4.5° (white dashed lines in the images, noted by Lat. = 4.5°) away from the equator. The magnitude of magnetic field in radial profile is given by subtracting its corresponding initial value of ambient equilibrium. The body of MC is identified to be enclosed by a white solid line in the images and between two dotted lines in attached profiles. The white solid line is determined by the magnetic flux function (ψ) value in the equator plus a small increment. This line lies right inside the MC boundary which has the flux function value equal to that in the equator. The MC core is determined by the maximum value of ψ. Magnetic field configuration is superimposed upon the images. As shown in the Figure 1, the MC ejection into ambient solar wind results in two distinct interaction regions: (1) an MC envelope composed of IMF draping around self-enclosed MC surface; (2) a shock front and its associated sheath ahead of MC body formed by the compression of the high-speed MC. A concave is formed at the MC-driven shock front across the HPS, as clearly seen in Figure 1(b), which is also substantiated by IPS (interplanetary scintillation) observation [Watanabe et al., 1989] and shock-related simulations [Odstrcil et al., 1996a, b; Hu and Jia, 2001]. The characteristics of shock front are caused by the particular HCS-HPS structure in heliosphere. Shock degenerates abruptly into hydrodynamic shock due to nearly vanishing magnetic field at neutral current sheet. So the fastest and strongest shock front locates on the edges of HPS instead of being right in HCS. The angular width of shock front is much larger than that of its driver–MC body. Monotonic decrease of bulk flow speed v_r in the MC, as seen from Figure 1(b), implies continuous MC expansion through IP space. Moreover, many other MC characteristics are also manifested in agreement with the observations. These characteristics maintain till the MC propagates beyond the outer boundary.

The in-situ measurement along Lat. $= 4.5°$ by a hypothetic spacecraft at L1 is shown in Figure 2. Typical MC characteristics, such as enhanced magnetic magnitude B (also in attached profiles in Figure 1(a)), smooth rotation of magnetic field Θ, a low concave of proton temperature T_p and proton beta β_p (also in attached profiles in Figure 1(c)), continuous decrease of bulk flow speed v_r (also in attached profiles in Figure 1(b)) and so on, are reproduced. A sheath ahead of the MC with high temperature and high speed is clearly seen too. The shock front, the leading, central and trailing parts of MC pass by L1 at 49.3, 60, 71 and 87.4 hours successively. The MC event at L1 lasts 27.4 hours, with a maximum magnetic field magnitude (17.9nT) and a minimum southward component (-7.7 nT). The geomagnetic effect of the simulated MC event is evaluated by Dst index, as applied by Wang et al. [2003c] using formula $\frac{dDst(t)}{dt} = Q(t) - \frac{Dst(t)}{\tau}$ [Burton et al., 1975], where the coupling function $Q = VB_s$ (here V is evaluated with v_r, $B_s = \min(B_z, 0)$ and B_z is the z component of magnetic field) and the diffusion time scale $\tau = 8$ hours. The MC center approaches L1 71 hours after its departure from the inner boundary, and the value of Dst index decreases monotonically to its minimum -86 nT shortly afterwards (at 88.6 hours). In addition, the draping IMF within MC-driven sheath is mainly northward.

This is why the compressed magnetic field in the sheath does not cause significant Dst disturbance in our simulation.

4. Interaction between a Fast Shock and a Preceding MC

4.1. Case B

Shock compression is an efficient mechanism for the enhancement of southward component of magnetic field and, hence, serves as an IP cause of large geomagnetic storms [Wang et al., 2003b, c]. The subsequent numerical simulations aim to quantify geoeffectiveness of a shock overtaking an MC in detail.

To investigate the interaction between a fast forward shock and a preceding MC, a shock centered at HCS ($\theta_{sc} = 0°$) is introduced from the inner boundary to pursue the previous occurred MC. The MC in this case is identical with that in Case A. The shock emerges at $t_{s0} = 41$ hours with its center on the equator, and other parameters

$$\Delta\theta_s = 6°, \quad R^* = 24, \quad t_{s1} = 0.3 \text{ hr}, \quad t_{s2} = 1 \text{ hr}, \quad t_{s3} = 0.3 \text{ hr}.$$

One can find that the maximum shock speed is 1630 kms^{-1} from the above quantities by the shock relation. The ratio of total pressure decreases from R^* at the equator to 1 at ±6° aside via a cosine function. The temporal extent, as already specified, can be described as being trapezoidal as done, for example, by Smith and Dryer [1990] in the ecliptic plane.

The detail process of MC-shock event is elucidated in Figure 3. The incidental shock aphelion and the MC core arrive at $80R_s$ and $155R_s$ respectively in 49.5 hours, shown in Figure 3(a), (d) and (g). The morphology of shock front has a dimple across HCS, similar to that of MC-driven shock mentioned previously. In the downstream of shock front, the flow speed reaches its maximum value, 900 kms^{-1}, 4.5° away from HCS, much greater than that right at HCS, which is 560 kms^{-1}. Comparing with the preceding MC, which has a peak speed of 540 kms^{-1} only, the overwhelming forward shock will soon collide with MC body. Moreover, the tangential magnetic field component increases as fast shock passes by. So that IMF in either semi-heliosphere is deflected to the pole by the impaction of shock propagation. As a result, a "magnetic vacuum" with weaker magnetic field strength nearby HCS is formed just behind the shock front, as indicated in Figure 3(a)-(c). The shock just catches up with the inner boundary of MC at 69.5 hours (Figure 3(b), (e) and (h)). In addition, as shown in Figure 3(h), the radial characteristic speed of fast mode wave c_f is very large in the MC body with low β. It increases steadily from 100 kms^{-1} at MC boundary to 200 kms^{-1} in maximum at MC core. There is also a peak value 180 kms^{-1} for c_f within the shock sheath. Meanwhile, v_r in the MC decreases monotonically from 540 kms^{-1} to 430 kms^{-1} along Lat. $= 0°$, as seen in Figure 3(e). MC-shock collision is pregnant at this critical time. Moreover (1) the aphelion of shock front locates on the edges of HPS instead of being right at HCS due to its concave morphology; (2) the incidental shock in HCS is virtually a relatively weaker hydrodynamic shock. Though the center of shock front is along HCS, the most violent collision can be witnessed consequently at shock aphelion rather than in HCS when the shock and MC collide with each other. A sharp discontinuity has already been formed in the rear part of MC at 81.5 hours (Figure 3(c), (f) and (i)). The compression along HCS (Lat. $= 0°$) is less significant than that along Lat. $= 4.5°$. The influence of fast shock upon MC could be reduced into two aspects: (1) enhancement of magnetic field magnitude; (2) rotation of magnetic field. As shown in Figure 3(c), the maximum value of magnetic field enhancement $(B - B|_{t=0})$

is 30 nT in compressed region, much larger than that at MC core, 18 nT. Compressed magnetic field lines are very flat and point nearly southwards. Both effects result in a minimum southward magnetic field B_z with -33 nT at MC tail. Furthermore, c_f is enhanced simultaneous during shock compression, as seen from Figure 3(i). In contrast with 160 kms^{-1} at MC core, c_f at MC tail has jumped to 300 kms^{-1}. However, the strong shock is not counteracted completely by the enhanced c_f in the MC medium. Its propagation in MC would not be stopped or diffused despite MC resistance. In addition, the domain of so-called "magnetic vacuum" behind shock front is magnified during the process of shock overtaking rear part of MC, because the MC, an enclosed magnetic loop, serves as an obstacle in front of shock. The MC just passes by L1 at 82 hours. Though shock continues to penetrate MC into a deeper position, MC-shock compound structure will no longer cause the geoeffectiveness shortly after it passes by the orbit of earth.

Similar to that in Case A, the simulated data at L1 in time sequence are shown in Figure 4. A bump on the tail of MC is obviously found around 81 hours, with a peak speed 660 kms^{-1} larger than 540 kms^{-1} at the head of MC. As a consequence, VB_z jumps from -4 mVm^{-1} to -21 mVm^{-1} for less than 2 hours. By comparing with Figure 2, one can see from Figure 4 that the index of geomagnetic storm Dst is -156 nT in MC-shock compound structure, much greater than -86 nT in the corresponding individual MC event. Moreover, the rear boundary of MC leaves L1 5.3 hours earlier than that in Case A. MC is highly compressed in its rear part by the shock.

4.2. Case C

To further explore the features of MC-shock interaction in solar-terrestrial range, we give another case of simulation (Case C) where the shock ultimately penetrates the preceding

MC nearby L1. It is straightforward to schedule an earlier shock emergence. The shock emergence time t_{s0} is modified to be 10 hours compared with 41 hours in Case B. All other parameters are the same as those in Case B.

Only the evolution of v_r is given in Figure 5, to visualize the concerned MC-shock complex structure. Once the fast shock advances deeply into the MC, the latter, superseding the ambient IP space, serves as a medium for the shock propagation. Since HCS does not exist in the MC, what ensues is the disappearance of the HCS-associated concave. The morphology of shock front is a smooth arc in the highly compressed rear part of MC at 20.6 hours (Figure 5(b)). When the shock penetrates and emerges from the MC, HCS-HPS structure re-plays an important role in shock propagation. The smooth arc quickly turns into a concave across the equator with respect to shock front at 52.1 hours, as indicated clearly by Figure 5(c). This newly emerged fast shock from the MC will gradually merges with the preceding MC-driven shock into a stronger fast shock by nonlinear interaction. Moreover, sheath width, defined by the radial distance along the equator between MC-driven shock front and the outer MC boundary, is $10R_s$ in Case C, only half of that in Case A, $20R_s$. Compared with Case A, several distinct differences are easily discriminated in Case C to emphasize the shock impact: (1) the geometry of MC boundary changes in the shape from quasi-circle to oblate ellipse; (2) MC is highly compressed; (3) the width of MC-driven sheath is significantly narrowed.

The hypothetic in-situ measurement at L1 along Lat. $= 4.5^\circ$ is plotted in Figure 6 in contrast. The outer boundary, the center, and the inner boundary of MC arrive at L1 at 55.5, 61 and 71.5 hours successively, which are 4.5, 10 and 15.9 hours earlier than those in Case A indicated by Figure 2. In presence of the shock penetration, the duration of MC passing across L1 is shortened by 11.4 hours. No extremum of speed profile is found inside the MC because the shock has moved out of it. Judged only from single-spacecraft in-situ observation, as seen from Figure 6, it resembles quite likely an individual MC event with a peak speed of ~ 620 kms^{-1}. The greatest compression occurs at the front of MC, with the maximum $B = 32$ nT, $VB_z = 19$ mVm^{-1}, the minimum $B_z = 31$ nT. However the highly compressed magnetic field is northward and makes no contribution to geomagnetic storm. This MC-shock event results in the geoeffectiveness with a value of $Dst = -107$ nT.

The comparison among Cases A and C about time-dependent parameters is shown in Figure 7. Firstly, heliospheric distance of MC core in Case A depends nearly linearly on time, as shown in Figure 7(a). The solar-terrestrial transporting speed of MC core is approximately 486 kms^{-1}. It suggests that an individual MC moves at a constant speed through IP medium, consistent with relevant simulations [Vandas et al., 1995, 1996b; Groth et al., 2000; Manchester et al., 2004a]. Meanwhile one can see that MC core in Case C is compressed by the shock, beginning from 20 hours. Secondly, MC boundary is not a exactly circle due to overall force balance at MC-ambient flow interface. MC diameter, defined as the radial distance difference between its inner and outer boundaries along HCS, is still used to quantify the size of MC. One can see that MC diameter increases monotonically to $73R_s$ at 1AU with an asymptotic radial expansion speed 93.7 kms^{-1} after 55 hours in Case A, as indicated by Figure 7(b). However, the angular width of MC in Case A behaves differently, as shown in Figure 7(c). It undergoes an initially rapid expansion from 15° to 27°, then gradually recovers to 23° at 1AU. Physical interpretation for the variance of MC width is as follows: (1) The MC abruptly expands at initial stage because its inherent magnetic field is overwhelming over that of the ambient solar wind.

(2) It contracts gradually afterwards while propagating in IP medium as its magnetic field decreases faster than that of IMF. Meanwhile, the diameter and width of MC in Case C is compressed by the shock, as indicated in Figure 7(b) and (c). Finally, the relationship between magnetic field magnitude in MC core and the time in Case A is also sought for the power ζ in $B \propto t^{-1/\zeta}$. ζ is about 0.76 in our model, consistent with relevant results [Vandas et al., 1995, 1996b]. The expansion of individual MC is pronounced from Figure 7, even on the condition of the adiabatic process $\gamma = 5/3$. Hence our simulation is in favor of the idea that $\gamma < 1$, proposed by Osherovich et al. [1993a, b, 1995], may not be a strict limitation for IP MC expansion [Vandas et al., 1996b, c; Vandas and Odstrcil, 2000; Skoug et al., 2000; Vandas, 2003].

Moreover the disturbance of speed enhancement just downstream of incidental shock front can not completely propagate into MC medium. After the shock front enters MC medium, the remaining high speed flow follows right after the inner boundary of preceding MC all the time, as seen from Figure 5(a)-(c), which can also be seen in the relevant simulation (Figure 3 in Vandas et al. [1997a]). The MC is highly compressed by the overtaking shock, as shown in Figure 7(b). The MC diameter decreases monotonically during shock passage in MC medium (14 $\sim$ 32 hrs). It then recovers gradually when shock penetrates and emerges from the MC ($>$ 32 hrs). Compared to relevant simulation (Figure 7(b) in Lugaz et al. [2005]), the behavior of MC diameter in our simulation differs only after shock emergence from MC medium. Because the forward shock in Lugaz et al. [2005] is driven by the following MC, the diameter of preceding MC remains constant by the compression of following MC body when the shock propagates at the front of preceding MC. With the push from above-mentioned high speed flow (Figure 5(a)-(c)) instead of following MC body, the MC diameter can not be completely recovered to that in corresponding individual MC event (Case A) after the passage of fast shock.

5. Geoeffectiveness Studies

Near-HCS latitudinal dependence of the Dst index is plotted in Figure 8. The Geomagnetic storm has been obviously aggravated by the shock overtaking the MC. The minimum Dst is found to be -103 nT in case A, -162 nT in case B, and -145 nT in case C. In Particular, the latitudinal distribution of Dst in Case B is nearly constant over Lat. $= -4^\circ \sim 4^\circ$. On the one hand, the southward passing magnetic flux decreases steadily away from the equator because the MC propagates along the HCS. On the other hand, the morphology of the shock front is a concave astride the heliospheric equator when the shock penetrates into the MC and has just begun to change, compared with a well-established smooth arc in Case C. The greatest compression occurs outside the equator. Two factors are balanced over a certain latitudinal width, thus resulting in the above-mentioned level distribution of Dst in Case B.

It is found from Cases B and C that the geoeffectiveness of MC-shock compound is undermined when shock penetrates completely through MC. To further study the dependence of Dst value on the penetration depth of shock overtaking MC, a set of numerical simulations with different duration between the emergence times of MC and shock are carried out. Seventeen cases are run with $t_{s0} =$ 3, 6, 10, 15, 20, 23, 26, 29, 32, 35, 38, 41, 44, 46, 48, 50, and 60 hours respectively.

By introducing a variable d_{Dst}, referring to the radial distance along heliospheric equator between shock front and the inner boundary of MC, we study the time-dependent data at L1 simultaneously recorded by two hypothetic spacecraft locating along Lat. $= 0^\circ$

and 4.5° respectively. The geoeffectiveness of MC-shock compound is described by Dst as an integral effect and minimum dawn-dusk electric field VB_z as an instant effect. Synthetical analyses on some crucial parameters are given in Figure 9, where the three vertical delimiting lines (dotted, dashed and dotted) from left to right correspond to the cases of shock encountering the tail, the core and the front of MC at L1, respectively. From top to bottom are plotted (a) the duration between the emergences of MC and shock from the inner boundary, noted by Dt, (b) the Dst index, (c) the minimum of dawn-dusk electric field VB_z, noted by Min.(VB_z), (d) the interval between the commencement of $VB_z < -0.5$ mV/m and the corresponding Dst minimum, noted by Δt, (e) the minimum of B_s, noted by Min.(B_s), (f) the maximum of magnetic field magnitude Max.(B), and (g) the arrival times of the MC and the shock along the equator, respectively. The solid and dashed lines in Figure 9(b)-(f) correspond to the hypothetic satellites located at Lat.=0° and 4.5°, respectively. It can be seen that MC and shock interact with each other and merge into a complex compound structure when $Dt < 50$ hours. The shock penetrates into the preceding MC more deeply with less duration between MC and shock emergences. Min.(B_s) and Min.(VB_z) decline sharply, especially along Lat. $= 4.5°$ as d_{Dst} increases from 0 to $11R_s$. Geoeffectiveness responses along Lat. $= 4.5°$ more dramatically due to the concave front of incidental shock. This results in almost the same Dst value over Lat. $= 0° \sim 4.5°$ for $d_{Dst} = 8 \sim 11R_s$. Obviously, the minimum Dst with -185 nT along Lat. $= 0°$ and -165 nT along Lat. $= 4.5°$ is obtained when the shock front just approaches MC core at L1, corresponding to $d_{Dst} = 23R_s$, as indicated by vertical dashed line of Figure 9. Moreover, Max.(B) remains constant during $d_{Dst} = 0 \sim 7R_s$, because increasing magnetic field magnitude at compressed region of MC is not yet comparable to that at MC core. The minimum of Min.(B_s) and Min.(VB_z) are obtained at a certain position in the rear part of MC. When the shock front exceeds the MC core and compresses its anterior part with $23R_s < d_{Dst} < 38.5R_s$, in which the magnetic field is northward, Dst recovers in different slopes along two latitudes. It recovers gradually from -185 to -175 nT along Lat. $= 0°$ but more rapidly from -165 to - 122 nT along Lat. $= 4.5°$. When $Dt < 20$ hours, the shock penetrates and propagates completely through the MC before L1. The region of dramatic interaction shifts from MC body to MC-driven sheath. As a result, magnetic field tension of MC body overcomes the grip of post-shock total pressure and Dst continues to recover monotonically as Dt decreases. In addition, the minimum of Δt (5 hours) and MC passage interval (13 hours) correspond to $d_{Dst} = 23$ and $38.5R_s$ respectively. In contrast with -103 nT along Lat. $= 0°$ in corresponding individual MC event, Dst reaches its minimum -185 nT along the same latitude with 80% increment in intensity when the shock front advances into MC core. Moreover, the shock transport time in MC-shock cases is shortened within $0R_s < d_{Dst} < 48R_s$ in contrast with that in the corresponding individual shock event, as indicated in Figure 9(g). The shortened time is 3.8 hours in maximum, corresponding to $d_{Dst} = 38.5R_s$. When the shock propagates from IP medium to MC medium, enhanced local magnetosonic speed and decreased bulk flow speed upstream shock front coexist. The joint effect of these two factors determines whether the shock is faster or slower in MC medium. Hence the propagation speed of incidental shock influenced by the MC depends on the interval between their commencements.

6. Concluding Remarks and Discussions

Using a 2.5D ideal MHD numerical model, MC-shock interaction and its geoeffectiveness are investigated for better understanding of the IP "shock overtaking MC" events [Wang et al., 2003b; Berdichevsky et al., 2005]. Our compound numerical algorithm is capable of capturing sharp shock front, ensuring the absence of magnetic monopole, guaranteeing the conservation of axial and toroidal magnetic flux of magnetic rope, and so on. The simulations reveal dynamic characteristics of IP MC-shock interaction and their associated geoeffectiveness in some aspects.

Firstly, numerical simulation is carried out on an individual MC with its inherent magnetic field overwhelming over that in the ambient flow. Characteristics of the specific MC propagation through IP space are summarized as follows: (1) The MC core propagates with a nearly constant speed; (2) Its diameter expands rapidly at initial stage. It then expands with a slower asymptotic speed; (3) Its angular width also expands rapidly at initial stage, but gradually contracts afterwards. Moreover, the characteristics of an MC, such as strong magnetic field, smooth rotation of magnetic field, low proton temperature, low plasma β, and so on, are quite in agreement with the observations.

Secondly, numerical simulation is conducted to model MC-shock interaction. A strong fast shock centered at HCS emerges from the inner boundary to pursue the preceding MC. It is found that the compression and rotation of magnetic field serve as an efficient mechanism to cause large geomagnetic storm. The fast shock initially catches up with the preceding MC. It then penetrates through the MC and finally merges with the MC-driven shock into a stronger compound shock. When the fast shock propagates through IP space, its front is characterized with a central concave shape in the equator; When it enters the preceding MC, its front evolves into a purely arc shape. The morphology of shock front is determined by the local medium. After the shock front enters MC medium, the remaining high speed flow just downstream of incidental shock front can not completely enter the preceding MC, and it just follows behind the MC all the time. The MC is highly compressed by the overtaking shock. The solar-terrestrial transport time of incidental shock relates closely to the duration between the emergences of MC and itself.

Lastly, the associated geoeffectiveness is studied based on numerical simulations. In contrast with the corresponding individual MC event, MC-shock interaction results in a largest geomagnetic storm with 80% increment in terms of Dst. Based on an analytical solution for the process of shock propagation from the inner boundary to the center of MC, Wang et al. [2003c] suggested that the maximum geomagnetic storm be caused by shock penetrating MC at a certain depth, and the stronger the incident shock is, the deeper is the position. Meanwhile, the incidental shock in our simulation is very strong and the results show that the maximum geomagnetic storm occurs when the shock front encounters MC core. Our numerical model agrees to some extent with that by Wang et al. [2003c]. Furthermore, the high speed flow right after the tail of MC boundary in our simulation mentioned previously might be responsible for the minor difference of shock penetration depth between the two models regarding the maximum geomagnetic storm.

One can see that the compressed sheath field ahead of MC in our simulations is generally northward and, hence, contribute little to geoeffectiveness (Figure 2, 4, 6). If both MC helicity and ambient IMF orientation are reversed, the magnetic field within MC-driven sheath and front part of MC will be directed southward and, hence, will be responsible for geomagnetic storm. Some of qualitative results compared to that discussed above can be straightforwardly conceived as follows: (1) Only when a shock propagates into the front of an MC does the shock exert its effect on geoeffectiveness; (2) A shock losses its energy and momentum heavily during its propagation through the rear part of an MC, so that it has relatively weaker influence on the geoeffectiveness by penetrating the preceding MC. Moreover, if an incidental shock is not strong enough, it may be dissipated quickly even in the rear part of an MC. Detailed quantitative investigation should resort to numerical simulation. This interesting topic will be addressed in near future.

Acknowledgments. We express our heartfelt thanks to the referees for their constructive comments. This work was supported by the National Natural Science Foundation of China (40274050, 40404014, 40336052, 40525014 and 40574063), and the Chinese Academy of Sciences (startup fund). M. Xiong was also supported by Innovative Fund of University of Science and Technology of China for Graduate Students (KD2005030).

References

Berdichevsky, D.B., I.G. Richardson, R.P. Lepping, and S.F. Martin (2005), On the origin and configuration of the 20 March 2003 interplanetary shock and magnetic cloud at 1 AU, *J. Geophys. Res.*, *110*, doi:10.1029/2004JA010662.

Burlaga, L.F., E. Sittler, F. Mariani, and R. Schwenn (1981), Magnetic loop behind an interplanetary shock: Voyager, helios, and IMP 8 observations, *J. Geophys. Res.*, *86(A8)*, 6,673–6,684.

Burlaga, L.F. (1988), Magnetic clouds and force-free fields with constant alpha, *J. Geophys. Res.*, *93*, 7,217-7,224.

Burlaga, L.F., S.P. Plunkett, and O.C.St. Cyr (2002), Successive CMEs and complex ejecta, *J. Geophys. Res.*, *107*, doi:10.1029/2001JA000255.

Burton, R.K., R.L. McPherron, and C.T. Russell (1975), An empirical relationship between interplanetary conditions and Dst, *J. Geophys. Res.*, *80*, 4,204.

Cane, H.V., I.G. Richardson, and G. Wibberenz (1997), Helios 1 and 2 observations of particle decreases, ejecta, and magnetic clouds, *J. Geophys. Res.*, *102*, 7,075.

Cho. K.-S., Y.-J. Moon, M. Dryer, A. Shanmugaraju, C.D. Fry, Y.-H. Kim, S.-C. Bong, and Y.-D. Park (2005), Examination of type II origin with SOHO/Lasco observations, *J. Geophys. Res.*, *110*, A12101, doi:10.1029/2004JA010744.

Cliver, E.W., S.W. Kahler, and D.V. Reames (2004), Coronal shocks and solar energetic proton events, *Astrophys. J., 605*, 902.

Dryer, M. (1996), Comments on the origins of coronal mass ejections, *Sol. Phys.*, *169*, 421–429.

Dryer, M. (1998), Multidimensional Magnetohydrodynamic simulation of solar-generated disturbances: space weather forecasting of geomagnetic storms, *AIAA. J.*, *36(3)*, 365–379.

Dryer, M., C.D. Fry, W. Sun, C. Deehr, Z. Smith, S.-I. Akasofu and M.D. Andrews (2001), Prediction in real time of the 2000 July 14 heliospheric shock wave and its companions during the 'Bastille' epoch, *Sol. Phys.*, *204*, 267–286.

Dryer, M., Z. Smith, C.D. Fry, W. Sun, C.S. Deehr, and S.-I. Akasofu (2004), Real time shock arrival predictions during the "Halloween 2003 epoch", *Space Weather*, *2*, S09001, doi:10.1029/2004SW000087.

Farrugia, C.J., L.F. Burlaga, V.A. Osherovich, I.G. Richardson, M.P. Freeman, R.P. Lepping, and A.J. Lazarus (1993), A study of an expanding interplanatary magnetic cloud and its interaction with the earth's magnetosphere - The interplanetary aspect, *J. Geophys. Res.*, *98(A5)*, 7,621-7,632.

Fry, C.D., W. Sun, C.S. Deehr, M. Dryer, Z. Smith, S.-I. Akasofu, M. Tokumaru, and M. Kojima (2001), Improvements to the HAF solar wind model for space weather predictions, *J. Geophys. Res.*, *106(A10)*, 20,985–21,001.

Fry, C.D., M. Dryer, Z. Smith, W. Sun, C.S. Deehr, and S.-I. Akasofu (2003), Forecasting solar wind structures and shock arrival times using an ensemble of models, *J. Geophys. Res.*, *108(A2)*, 1070, doi:10.1029/2002JA009474.

Fry, C.D., M. Dryer, W. Sun, T.R. Detman, Z.K. Smith, C.S. Deehr, C.-C. Wu, S.-I. Akasofu, and D.B. Berdichevsky (2004), Solar observation-based model for multiday predictions of interplanetary shock and CME arrivals at Earth, *IEEE Trans. Plasma Phys.*, *32(4)*, 1,489–1,497.

Fry, C.D., M. Dryer, W. sun, C.S. Deehr, Z. Smith, T.R. Detman, A. Aran, D. Lario, B. Sanahuja, and S.-I. Akasofu (2005), Key links in space weather: forecasting solar-generated shocks and proton acceleration, *AIAA. J.*, *43(5)*, 987–993.

Goldstein, H. (1983), On the field configuration in magnetic clouds, in *JPL Solar Wind Five*, NASA Conf. Publ. 2280, Washington D.C., p. 731-733.

Gonzalez-Esparza, A., A. Santillan, and J. Ferrer (2004), A numerical study of the interaction between two ejecta in the interplanetary medium: one- and two-dimensional hydrodynamic simulations, *Ann. Geophys.*, *22*, 3,741–3,749.

Gosling, J.T. (1990), Coronal mass ejections and magnetic flux ropes in interplanetary space, in *Physics of magnetic flux ropes*, edited by C.T. Russell, E.R. Priest, and L.C. Lee, *Geophys. Monogr. Ser.*, 58, P. 343, AGU.

Gosling, J.T. (1993), The solar flare myth, *J. Geophys. Res.*, *98(A11)*, 18,937.

Gosling, J.T., and A.J. Hundhausen (1995), Reply, *Sol. Phys.*, *160*, 57–60.

Groth, C.P.T., D.L. De Zeeuw, T.I. Gombosi, and K.G. Powell (2000), Global three-dimensional MHD simulation of a space weather event: CME formation, interplanetary propagation, and interaction with the magnetosphere, *J. Geophys. Res.*, *105(A11)*, 25,053–25,078.

Harten, A. (1983), High resolution schemes for hyperbolic conservation laws, *J. Comput. Phys.*, *49*, 357–393.

Hu, Y.Q. (1998), Asymmetric propagation of flare-generated shocks in the heliospheric equatorial plane, *J. Geophys. Res.*, *103(A7)*, 14,631–14,641.

Hu, Y.Q., and X.Z. Jia (2001), Interplanetary shock interaction with the heliospheric current sheet and its associated structures, *J. Geophys. Res.*, *106(A12)*, 29,299–29,304.

Hu, Y.Q., G.Q. Li, and X.Y. Xing (2003), Equilibrium and catastrophe of coronal flux ropes in axisymmetrical magnetic field, *J. Geophys. Res.*, *108*, 1,072.

Intriligator, D.S., W. Sun, M. Dryer, C.D. Fry, C. Deehr, and J. Intriligator (2005), From the Sun to the outer heliosphere: Modeling and analyses of the interplanetary propagation of the October/November (Halloween) 2003 solar events, *J. Geophys. Res.*, *110*, A09S10, doi:10.1029/2004JA010939.

Jeffrey, A., and T. Taniuti (1964), Non-linear wave propagation with application to physics and magnetohydrodynamics, New York, *Academic Press*.

Klein, L.W., and L.F. Burlaga (1982), Interplanetary magnetic clouds at 1 AU, *J. Geophys. Res.*, *87*, 613–624.

Kumar, A., and D.M. Rust (1996), Interplanetary magnetic clouds, helicity conservation, and current-core flux-ropes, *J. Geophys. Res.*, *101*(A7), 15,667-15,684.

Larson, D.E., R.P. Lin, J.M. McTiernan, J.P. McFadden, R.E. Ergun, M. McCarthy, H. Reme, T.R. Sanderson, M. Kaiser, R.P. Lepping, and J. Mazur (1997), Tracing the topology of the October 18-20, 1995, magnetic cloud with $\sim 0.1 - 10^2$ keV electrons *Geophys. Res. Lett.*, *24*(15), 1,911–1,914.

Lugaz, N., W.B. Manchester IV, and T.I. Gombosi (2005), Numerical simulation of the interaction of two coronal mass ejections from sun to earth, *Astrophys. J., 634*, 651–662.

Lundquist, S. (1950), Magnetohydrostatic fields, *Ark. Fys.*, *2*, 361–365.

Manchester, W.B., T.I. Gombosi, I. Roussev, D.L. De Zeeuw, I.V. sokolov, K.G. Powell, G. Toth, and M. Opher (2004a), Three-dimensional MHD simulation of a flux rope driven CME, *J. Geophys. Res.*, *109*, A01102, doi:10.1029/2002JA009672.

Manchester, W.B., T.I. Gombosi, I. Roussev, A. Ridley, D.L. De Zeeuw, I.V. sokolov, K.G. Powell, and G. Toth (2004b), Modeling a space weather event from the Sun to the Earth: CME generation and interplanetary propagation, *J. Geophys. Res.*, *109*, A02107, doi:10.1029/2003JA010150.

McKenna-Lawlor, S.M.P., M. Dryer, Z. Smith, K. Kecskemety, C.D. Fry, W. Sun, C.S. Deehr, D. Berdichevsky, K. Kudela, and G. Zastenker (2002), Arrival times of flare/halo CME associated shocks at the Earth: comparison of the precdictions of three numerical models with these observations, *Ann. Geophys.*, *20*, 20,917–20,935.

McKenna-Lawlor, S.M.P., M. Dryer, C.D. Fry, W. Sun, D. Lario, C.S. Deehr, B. Sanahuja, V.A. Afonin, M.I. Verigin, and G.A. Kotova (2005), Predictions of energetic particle radiation in the close Martian environment, *J. Geophys. Res.*, *110*, A03102, doi:10.1029/2004JA010587.

Odstrcil, D., Z. Smith, and M. Dryer (1996a), Distortion of the heliospheric plasma sheet by interplanetary shocks, *Geophys. Res. Lett.*, *23*, 2,521.

Odstrcil, D., M. Dryer and Z. Smith (1996b), Propagation of an interplanetary shock along the heliospheric plasma sheet, *J. Geophys. Res.*, *101(A9)*, 19,973–19,986.

Odstrcil, D., J.A. Linker, R. Lionello, Z. Mikic, P. Riley, V.J. Pizzo, and J.G. Luhmann (2002), Merging of coronal and heliospheric numerical two-dimensional MHD models, *J. Geophys. Res.*, *107(A12)*, SSH 14-1, doi: 10.1029/2002JA009334.

Odstrcil, D., M. Vandas, V.J. Pizzo, P. MacNeice (2003), Numerical Simulation of Interacting Magnetic Flux Ropes, in *AIP Conf. Proc. 679, Solar Wind 10*, edited by M. Velli, R. Bruno, and F. Malara, p. 699-702.

Osherovich, V.A., C.J. Farrugia, and L.F. Burlaga (1993a), Nonlinear evolution of magnetic flux ropes, 1. low-beta limit, *J. Geophys. Res.*, *98*, 13,225.

Osherovich, V.A., C.J. Farrugia, and L.F. Burlaga (1993b), Dynamics of aging magnetic clouds, *Adv. Space Res.*, *13*, 57.

Osherovich, V.A., C.J. Farrugia, and L.F. Burlaga (1995), Nonlinear evolution of magnetic flux ropes, 1. finite-beta plasma, *J. Geophys. Res.*, *100*, 12,307.

Osherovich, V.A. and L.F. Burlaga (1997), Magnetic clouds, in *Coronal mass ejections*, edited by N. Crooker, J.A. Joselyn, and J. Feynman, *Geophys. Monogr. Ser.*, Vol. *99*, p. 157, AGU.

Powell, K.G., P.L. Roe, R.S. Myong, T. Gombosi, and D. de Zeeuw (1995), An upwind scheme for magnetohydrodynamics, in *AIAA 12th Computational Fluid Dynamics conference*, San Diego, CA, p. 661.

Raouafi, N.E., S. Mancuso, S.K. Solanki, B. Inhester, M. Mierla, G. Stenborg, J.P. Delaboudiniere and C. Benna (2004), Shock wave driven by an expanding system of loops, *Astron. Astrophys.*, *424*, 1,039.

Ryu, D., and T.W. Jones (1995), Numerical magnetohydrodynamics in astrophysics: algorithm and tests for one-dimensional flow, *Astrophys. J.*, *442*, 228–258.

Schmidt, J.M., and P.J. Cargill (2003), Magnetic reconnection between a magnetic cloud and the solar wind magnetic field, *J. Geophys. Res.*, *108(A1)*, 1,023, doi:10.1029/2002JA009325.

Shu, C.W. (1997), Essentially Non-oscillatory and Weighted Essentially Non-oscillatory Schemes for Hyperbolic Conservation Laws, *ICASE Report*, 97–65.

Skoug, R.M., W.C. Feldman, J.T. Gosling, D.J. McComas, and C.W. Smith (2000), Solar wind electron characteristics inside and outside coronal mass ejections, *J. Geophys. Res.*, *105(A10)*, 23,069–23,084.

Smart, D.F., and M.A. Shea (1985), A simplified model for timing the arrival of solar flare-initiated shocks, *J. Geophys. Res.*, *90*, 183–190.

Smith, Z., and M. Dryer (1990), MHD study of temporal and spatial evolution of simulated interplanetary shocks in the ecliptic plane within 1 AU, *Sol. Phys.*, *129*, 387–405.

Svestka, Z. (1995), On 'the solar flare myth' postulated by Gosling, *Sol. Phys.*, *160*, 53–56.

Vandas, M., S. Fischer, M. Dryer, Z. Smith, and T. Detman (1995), Simulation of magnetic cloud propagation in the inner heliosphere in two dimensions 1. A loop perpendicular to the ecliptic plane, *J. Geophys. Res.*, *100(A7)*, 12,285–12,292.

Vandas, M., S. Fischer, M. Dryer, Z. Smith, and T. Detman (1996a), Simulation of magnetic cloud propagation in the inner heliosphere in two dimensions 2. A loop parrallel to the ecliptic plane and the role of helicity, *J. Geophys. Res.*, *101(A2)*, 2,505–2,510.

Vandas, M., S. Fischer, M. Dryer, Z. Smith, and T. Detman (1996b), Parametric study of loop-like magnetic cloud propagation, *J. Geophys. Res.*, *101(A7)*, 15,645–15,652.

Vandas, M., S. Fischer, P. Pelant, M. Dryer, Z. Smith, and T. Detman (1996c), MHD simulation of the propagation of loop-like and bubble-like magnetic clouds, in *AIP Conf. Proc. 382, Solar Wind 8*, p. 566–569.

Vandas, M., S. Fischer, M. Dryer, Z. Smith, T. Detman, and A. Geranios (1997a), MHD simulation of an interaction of a shock wave with a magnetic cloud, *J. Geophys. Res.*, *102(A10)*, 22,295–22,300.

Vandas, M., S. Fischer, D. Odstrcil, M. Dryer, Z. Smith, and T. Detman (1997b), Flux ropes and spheromaks: A numerical study, in *Coronal mass ejections*, edited by N. Crooker, J.A. Joselyn, and J. Feynman, *Geophys. Monogr. Ser.*, Vol. *99*, p. 169-176, AGU.

Vandas, M., and D. Odstrcil (2000), Magnetic cloud evolution: a comparison of analytical and numerical solutions, *J. Geophys. Res.*, *105(A6)*, 12,605–12,616.

Vandas, M., D. Odstrcil, and S. Watari (2002), Three-dimensional MHD simulation of a loop-like magnetic cloud in the solar wind, *J. Geophys. Res.*, *107(A9)*, SSH 2-1, doi:10.1029/2001JA005068.

Vandas, M. (2003), Interplanetary modeling of ICMEs, in *Proc. ISCS 2003 Symposium*, 'Solar Variability as an Input to the Earth's Environment', ESA SP-535, p. 527–534.

Vandas, M., and D. Odstrcil (2004), Acceleration of electrons by interacting CMEs, *Astron. Astrophys.*, *415*, 755-761.

Vassiliadis, D., A.J. Klimas, J.A. Valdivia, and D.N. Baker (1999), The Dst geomagnetic response as a function of storm phase and amplitude and the solar wind electric field, *J. Geophys. Res.*, *104*, 24,957.

Wang, Y.M., S. Wang and P.Z. Ye (2002), Multiple magnetic clouds in interplanetary space, *Sol. Phys.*, *211*, 333–344.

Wang, Y.M., P.Z. Ye and S. Wang (2003a), Multiple magnetic clouds: Several examples during March - April, 2001, *J. Geophys. Res.*, *108*(A10), 1370, doi:10.1029/2003JA009850.

Wang, Y.M., P.Z. Ye, S. Wang, and X.H. Xue (2003b), An interplanetary cause of large geomagnetic storms: Fast forward shock overtaking preceding magnetic cloud, *Geophys. Res. Lett., 30*(13), 1,700, doi:10.1029/2002GL016861.

Wang, Y.M., P.Z. Ye, S. Wang, and M. Xiong (2003c), Theoretical analysis on the geoeffectiveness of a shock overtaking a preceding magnetic cloud, *Sol. phys., 216*, 295–310.

Wang, Y.M., H.N. Zheng, S. Wang, and P.Z. Ye (2005), MHD Simulation on Formation and Propagation of Multiple Magnetic Clouds in the Heliosphere, *Astron. Astrophys.*, *434*, 309-316.

Watanabe, T., T. Kakinuma, M. Kojima, and R. schwenn (1989), Large-scale propagation properities of an interplanetary disturbances in association with a "halo" coronal mass ejection on 27 November 1979, *Nagoya Univ. Proc. Res. Inst. Atmos.*, *36*, 11.

Webb, D.F., T.G. Forbes, H. Aurass, J. Chen, P. Martens, B. Rompolt, V. Rusin, S.F. Martin, and V. Gaizauskas (1994), Material ejection: Report of the flares 22 workshop held at Ottawa, Canada, May 1993, *Sol. Phys.*, *153*, 73.

Winterhalter, D., E.J. Smith, M.E. Burton, and N. Murphy (1994), The heliospheric plasma sheet, *J. Geophys. Res.*, *99*, 6,667.

Zhang, Y.Z., Y.Q. Hu, and J.X. Wang (2005), Double catastrophe of coronal flux rope in quadrupolar magnetic field, *Astrophys. J., 626*(7), 1,096–1,101.

Figure Captions

Figure 1 One snapshot of a typical MC near L1 for Case A. (a) Magnetic field magnitude B, (b) radial flow speed v_r, and (c) proton beta β_p are illustrated with two additional radial profiles along Lat. $= 0^\circ$ and 4.5° respectively. Note: radial profile of B is plotted by subtracting initial ambient value $B|_{t=0}$. The white solid line in each image denotes the boundary of MC. The difference of magnetic flux function $\Delta\psi$ between adjoining magnetic field lines in and out of the MC are 5.9×10^{12} and 7.9×10^{12} Wb. Solid and dashed lines at each profile denote the core and boundary of MC. [*See the electronic edition of the Journal for a color version of this figure.*]

Figure 2 The in-situ measurements along Lat.$= 4.5^\circ$ by a hypothetic spacecraft at L1 for Case A. Magnetic field magnitude B, elevation of magnetic field Θ, radial flow speed v_r, proton beta β_p, proton temperature T_p, calculated dawn-dusk electric field VB_z, and Dst index are plotted in stacked panels. Solid and dashed vertical lines denote the center and boundary of MC.

Figure 3 The evolution of shock overtaking MC for Case B, with (a)-(c) magnetic field magnitude B, (d)-(f) radial flow speed v_r, and (g)-(i) radial characteristic speed of fast mode c_f. Below each image are two attached radial profiles along Lat.$= 0^\circ$ and 4.5°.

Note: spatial profile of B is plotted by subtracting initial ambient value $B|_{t=0}$. [*See the electronic edition of the Journal for a color version of this figure.*]

Figure 4 The in-situ measurements along Lat. $= 4.5°$ by a hypothetic spacecraft at L1 for Case B.

Figure 5 The evolution of shock overtaking MC for Case C with radial flow speed v_r. Only part of domain is plotted to highlight MC in (a) and (b). [*See the electronic edition of the Journal for a color version of this figure.*]

Figure 6 The in-situ measurements along Lat.$= 4.5°$ by a hypothetic spacecraft at L1 for Case C.

Figure 7 The time dependence of MC parameters: (a) radial distance of MC core, (b) MC diameter, (c) MC angular width. The solid and dashed lines denote individual MC event (Case A) and MC-shock event (Case C). Two vertical dashed lines denote when the shock front arrives at the rear and front of MC.

Figure 8 The comparison of latitudinal distribution of Dst index among individual MC event (Case A) and MC-shock events (Cases B and C). The solid, dashed, and dashed-dotted lines denote Case A, B, C respectively.

Figure 9 The parameter variances of MC-related geoeffectiveness as a function of d_{Dst}. Here d_{Dst} refers to radial distance between shock front and inner MC boundary along heliospheric equator. From left to right, three vertical lines (1st dotted, dashed, 2nd dotted) denote the critical situations of shock just reaching the tail, the core, and the front of preceding MC at L1 respectively. The mark Δ and $\times$ denote corresponding numerical results of Case B and C. (a) Dt, the duration between the emergences of MC and shock from the inner boundary, (b) Dst index, (c) Min.(VB_z), the minimum of dawn-dusk electric field VB_z, (d) Δt, the interval between the commencement of $VB_z < -0.5$ mV/m and the corresponding Dst minimum, (e) Min.(Bs), the minimum of southward magnetic component, (f) Max.(B), the maximum of magnetic magnitude and (g) arrival times of the MC and the shock along the equator, respectively. Solid and dashed lines in (b) to (f) correspond to observations along Lat.=0° and 4.5°. Arrival times of the outer and inner boundaries of MC, as well as that of incidental shock in MC-shock event and corresponding individual shock event are indicated by dashed-dotted and dashed-dotted-dotted, as well as solid and dashed lines in (g) respectively.

Table 1. Physical parameters of ambient solar wind at the bottom ($25R_s$) and at Lagrangian point $L1$ ($213R_s$)

Variable	Description	$25R_s$	$213R_s$
$N_p(\mathrm{cm}^{-3})$	proton number density	550	8
v_r(km/s)	radial speed	375	452
B(nT)	magnetic field strength	400	6.4
β	thermal to magnetic pressure ratio	0.23	0.93
$T_p(10^5K)$	proton Temperature	9.6	0.7
c_f(km/s)	radial fast characteristic speed	372	61

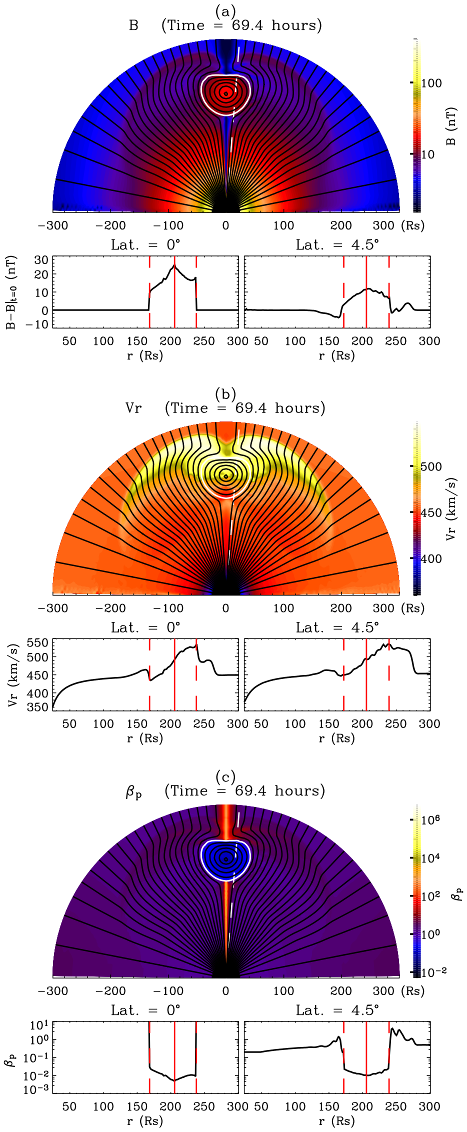
(a)
B (Time = 69.4 hours)
100
10
B (nT)
−300 −200 −100 0 100 200 300 (Rs)
Lat. = 0°
Lat. = 4.5°
B−B|t=0 (nT)
30 20 10 0 −10
50 100 150 200 250 300
r (Rs)
(b)
Vr (Time = 69.4 hours)
500
450
400
Vr (km/s)
550 500 450 400 350
(c)
βp (Time = 69.4 hours)
10^6
10^4
10^2
10^0
10^−2
βp
10^1 10^0 10^−1 10^−2 10^−3

Figure 1.

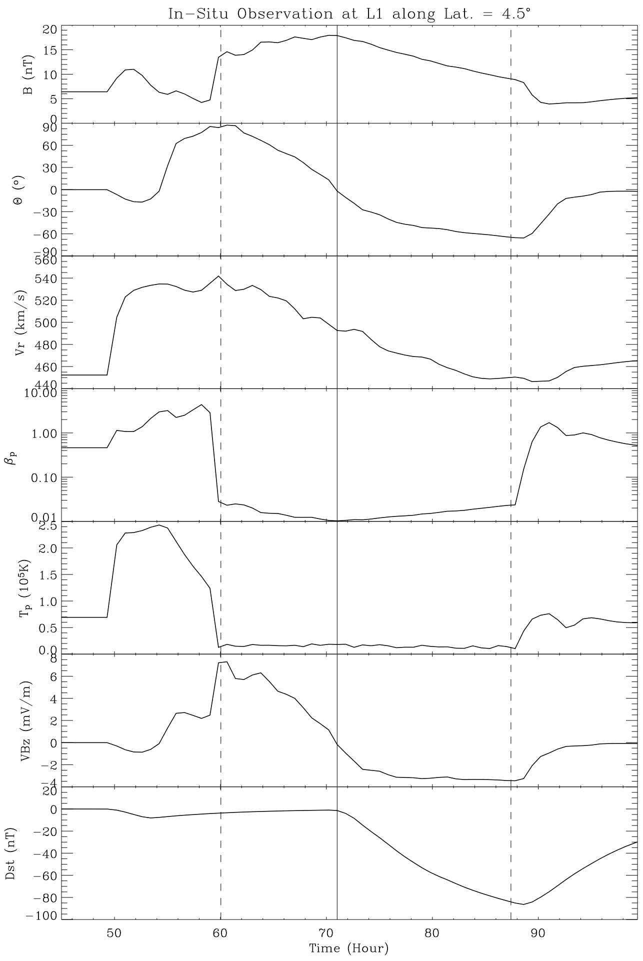
In−Situ Observation at L1 along Lat. = 4.5°
B (nT)
20
15
10
5
0
θ (°)
90
60
30
0
−30
−60
−90
Vr (km/s)
560
540
520
500
480
460
440
β_p
10.00
1.00
0.10
0.01
T_p (10^5K)
2.5
2.0
1.5
1.0
0.5
0.0
VBz (mV/m)
8
6
4
2
0
−2
−4
Dst (nT)
20
0
−20
−40
−60
−80
−100
50
60
70
80
90
Time (Hour)

Figure 2.

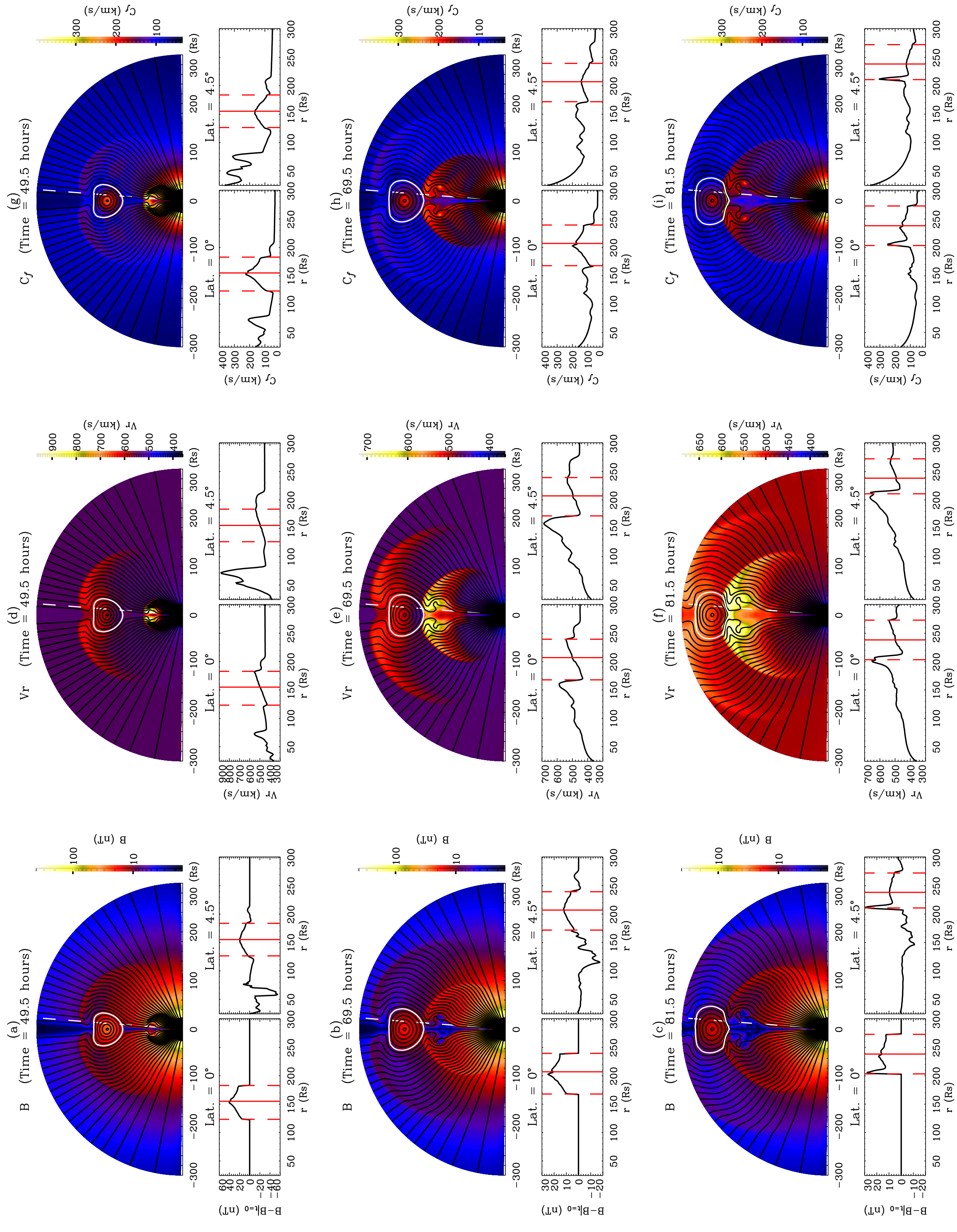
(a) B (Time = 49.5 hours)
(b) B (Time = 69.5 hours)
(c) B (Time = 81.5 hours)
(d) Vr (Time = 49.5 hours)
(e) Vr (Time = 69.5 hours)
(f) Vr (Time = 81.5 hours)
(g) C_f (Time = 49.5 hours)
(h) C_f (Time = 69.5 hours)
(i) C_f (Time = 81.5 hours)
B (nT)
Vr (km/s)
C_f (km/s)
$B-B|_{t=0}$ (nT)
Lat. = 0°
Lat. = 4.5°
r (Rs)
(Rs)
−300
−200
−100
0
100
200
300

Figure 3.

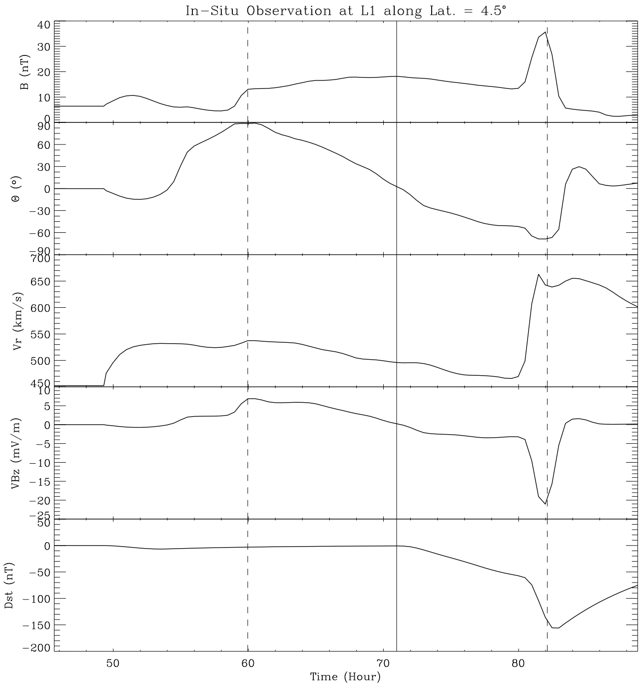
In−Situ Observation at L1 along Lat. = 4.5°
B (nT)
0
10
20
30
40
θ (°)
−90
−60
−30
0
30
60
90
Vr (km/s)
450
500
550
600
650
700
VBz (mV/m)
−25
−20
−15
−10
−5
0
5
10
Dst (nT)
−200
−150
−100
−50
0
50
50
60
70
80
Time (Hour)

Figure 4.

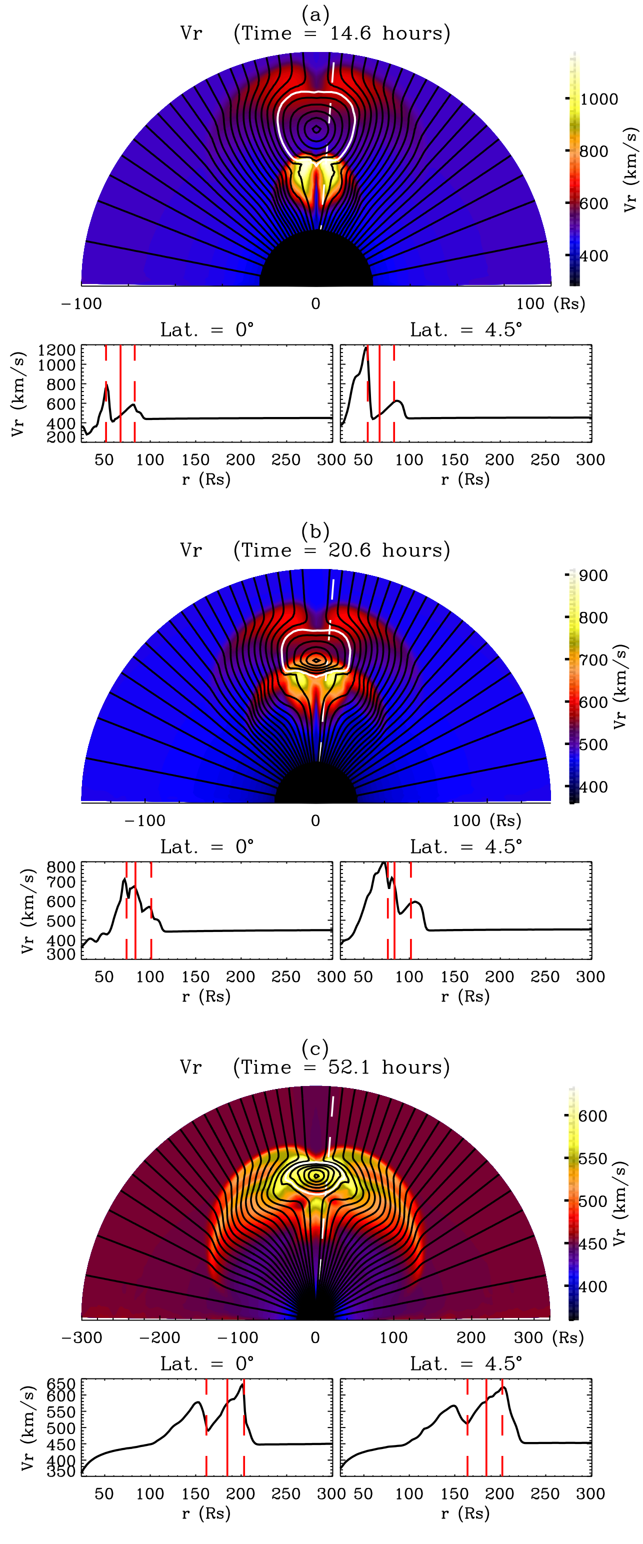
(a)
Vr (Time = 14.6 hours)
1000
800
600
400
Vr (km/s)
−100
0
100 (Rs)
Lat. = 0°
Lat. = 4.5°
1200
1000
800
600
400
200
Vr (km/s)
50 100 150 200 250 300
r (Rs)
(b)
Vr (Time = 20.6 hours)
900
800
700
600
500
400
Vr (km/s)
−100
0
100 (Rs)
Lat. = 0°
Lat. = 4.5°
800
700
600
500
400
300
Vr (km/s)
50 100 150 200 250 300
r (Rs)
(c)
Vr (Time = 52.1 hours)
600
550
500
450
400
Vr (km/s)
−300 −200 −100 0 100 200 300 (Rs)
Lat. = 0°
Lat. = 4.5°
650
600
550
500
450
400
350
Vr (km/s)
50 100 150 200 250 300
r (Rs)

Figure 5.

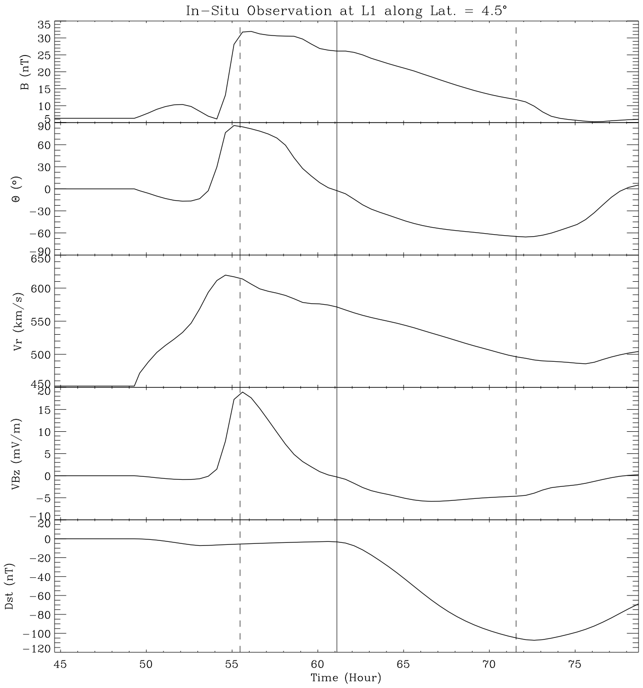
In–Situ Observation at L1 along Lat. = 4.5°
B (nT)
35
30
25
20
15
10
5
θ (°)
90
60
30
0
−30
−60
−90
Vr (km/s)
650
600
550
500
450
VBz (mV/m)
20
15
10
5
0
−5
−10
Dst (nT)
20
0
−20
−40
−60
−80
−100
−120
45
50
55
60
65
70
75
Time (Hour)

Figure 6.

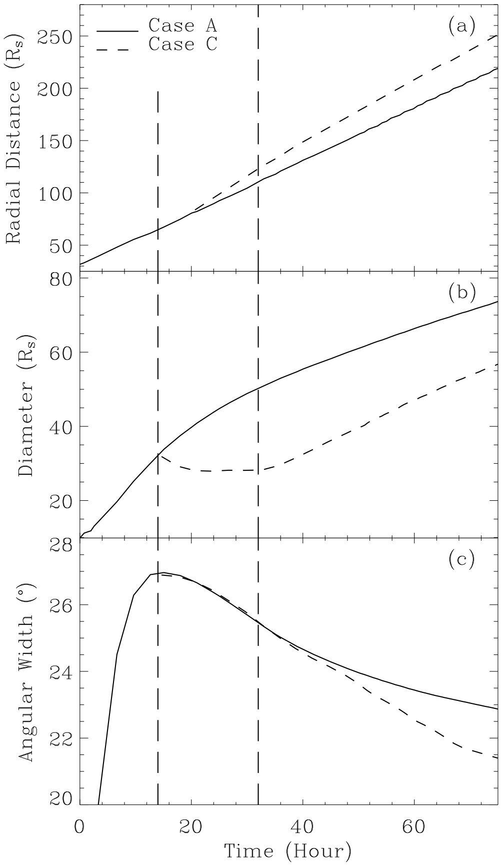

Figure 7.

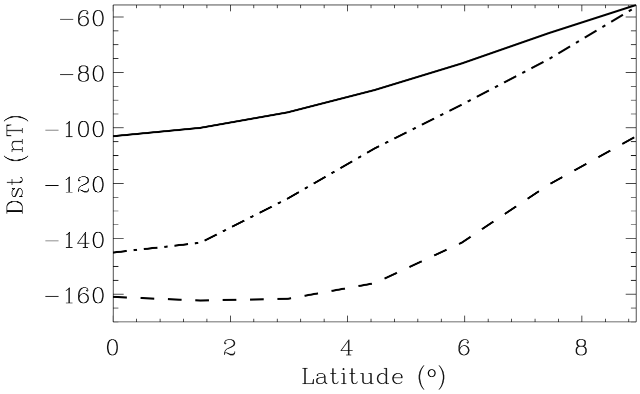

Figure 8.

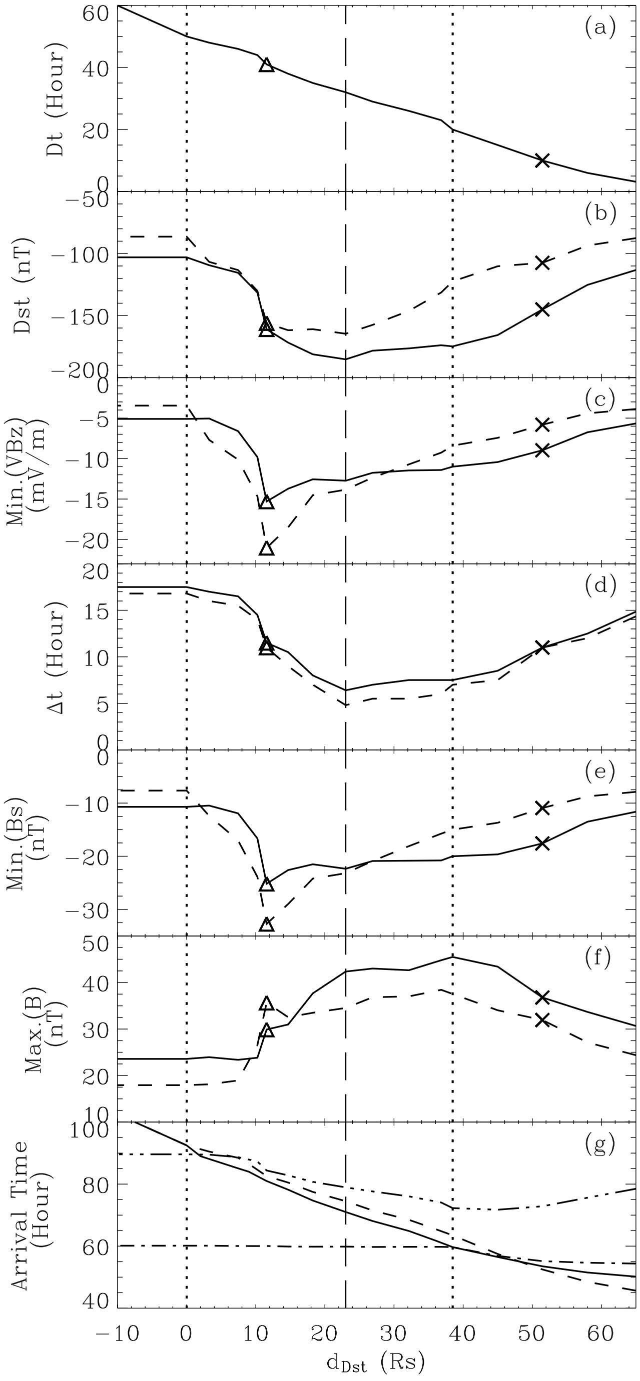
(a)
Dt (Hour)
60
40
20
0
(b)
Dst (nT)
−50
−100
−150
−200
(c)
Min.(VBz) (mV/m)
0
−5
−10
−15
−20
(d)
Δt (Hour)
20
15
10
5
0
(e)
Min.(Bs) (nT)
0
−10
−20
−30
(f)
Max.(B) (nT)
50
40
30
20
10
(g)
Arrival Time (Hour)
100
80
60
40
−10
0
10
20
30
40
50
60
d_{Dst} (Rs)

Figure 9.